*Materials Science Forum*
*ISSN: 1662-9752, Vol. 1183, pp 35-44*
*doi:10.4028/p-Sau95E*

*Submitted: 2025-12-18*
*Revised: 2026-02-12*
*Accepted: 2026-02-24*
*Online: 2026-04-13*

# A Novel Modified SLAB Method Approach for Efficient Energy Assessment in Ring Rolling Showing Fishtail Effect

Cristian Cappellini[1,a*], Claudio Giardini[1,b], Gabriele Locatelli[1,c] and Mariangela Quarto[1,d]

[1]Department of Management, Information and Production Engineering, University of Bergamo, Via Pasubio 7/b, 24044, Dalmine, Italy

[a*]cristian.cappellini@unibg.it, [b]claudio.giardini@unibg.it, [c]gabriele.locatelli@unibg.it, [d]mariangela.quarto@unibg.it

*corresponding author: cristian.cappellini@unibg.it

**Keywords:** ring rolling, fishtail effect, FEM, slab method.

**Abstract.** Ring rolling (RR) is a widely used process for producing seamless rings, but its complex thermo-mechanical behavior often requires costly experiments or FEM simulations. This study presents a novel analytical method for predicting torque and energy in RR that explicitly accounts for the fishtail effect, a lateral deformation of the ring cross-section. The approach combines a slab-based mechanistic model with a regression linking fishtail deformation to the kinematic ratio between mandrel feed and ring rotation. Validation was performed via FEM simulations on an industrial AISI 1045 steel case, covering thirty conditions with varying feed rates and rotational speeds. Results show that conventional models ignoring fishtail can overestimate errors by over 60% for torque and 50% for energy, whereas the proposed method reduces errors below 15% in most cases. These findings highlight the importance of including fishtail effects, offering a fast, reliable, and efficient tool for early-stage RR process design and optimization.

## Introduction

Ring rolling (RR) is a rotary forming process widely used for manufacturing seamless rings. Compared with conventional roll-bending techniques, RR eliminates welding operations and enables the processing of a broad range of materials, including steels and alloys that are difficult to weld [1,2]. For these reasons, it is extensively applied in aerospace, automotive, energy, and bearing industries to produce components such as turbine rings, gear blanks, and bearing races [3]. RR is performed using specialized equipment consisting of a driving roll, which provides torque and rotation, a radial mandrel that compresses the workpiece, and a pair of conical axial rolls. The coordinated motion of these tools increases the ring diameter while simultaneously reducing its height and thickness until the desired geometry is achieved [4]. Despite its industrial relevance, RR process analysis remains challenging due to the strong coupling of thermo-mechanical phenomena, complex material flow, and continuously evolving contact conditions [5]. As a result, reliable estimation of loads, torque, and energy consumption typically relies on experimental trials or finite element method (FEM) simulations, which are costly and time-consuming [6]. This represents a major limitation in industrial practice, where rapid and accurate predictions are required during process design. To address these challenges, several analytical models have been proposed to describe RR mechanics. Slip-line-based approaches adapted from shape rolling theory have been used to estimate forces and torque under the small instantaneous reductions typical of RR [7]. Other analytical frameworks focus on contact interface estimation and rolling force prediction for kinematic optimization of mandrel and axial rolls [8]. In addition, the slab method has demonstrated good accuracy in predicting the evolution of rolling loads and torques [9]. However, most existing analytical approaches neglect the fishtail effect, which arises from non-uniform deformation along the ring height and causes localized bulging at the axial ends. Previous studies have identified mandrel feed rate, roll geometry, lubrication conditions, and the kinematic ratio between mandrel feed and ring rotational speed as the main factors influencing

fishtail formation [10]. Nevertheless, analytical models that explicitly incorporate this effect are still lacking.

In this context, the present work proposes a novel analytical methodology for predicting torque and energy consumption in RR. The approach extends the classical slab formulation by introducing a regression-based correction that accounts for fishtail-induced lateral deformation as a function of the kinematic ratio. The methodology is implemented in a dedicated computational framework and validated through FEM simulations on an industrial RR case [11], demonstrating improved accuracy and reliability in predicting key process parameters.

## The Proposed Methodology

The RR setup (Fig. 1a) consists of a driving roll, a mandrel, and a pair of conical axial rolls, each governed by independently programmed kinematics. During the RR process, the ring is rotated at an angular velocity $\omega_r$ [rad/s] by the driving roll, which operates at an angular speed $\omega_{DR}$ [rad/s]. Concurrently, the mandrel is radially fed toward the driving roll at a rate $f$ [mm/s], thereby reducing the initial ring width $w_i$ [mm]. The initial ring height $h_i$ [mm] is controlled by axially feeding the upper axial roll toward the lower one at a rate $f_{AR}$ [mm/s]. As a result of these combined motions, both the initial internal diameter $d_i$ [mm] and the external diameter $D_i$ [mm] of the ring progressively increase until the target geometry is achieved, defined by the final width $w_f$ [mm], height $h_f$ [mm], and internal and external diameters $d_f$ [mm] and $D_f$ [mm], respectively (Fig. 1b).

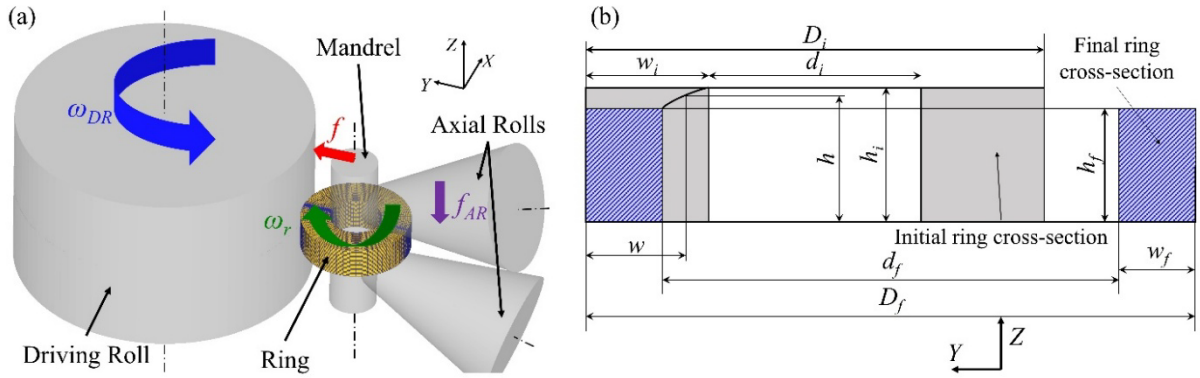


**Fig. 1.** Ring rolling setup (a) and ring cross-section evolution (b).

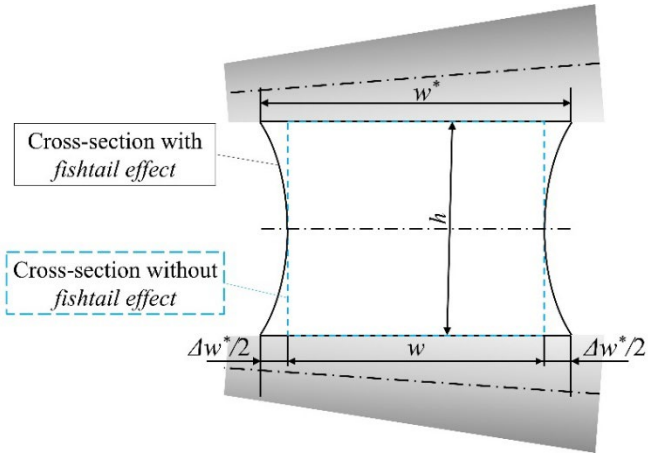


**Fig. 2.** Ring cross-section deformation due to the fishtail effect.

Owing to the closing motion of the rolls during RR, the ring cross-section undergoes increasing lateral spreading, commonly referred to as the fishtail defect [12], rather than maintaining an ideal rectangular shape. Fig. 2 compares the ring cross-sections obtained with (solid line) and without (dashed line) the fishtail effect and illustrates the parameters adopted for its quantification. These include the central cross-section width $w$ [mm], the enlarged widths at the top and bottom $w^*$ [mm],

and their difference, defined as the spread difference $\Delta w^*$ [mm]. This lateral deformation of the cross-section leads to an increase in rolling torque and energy consumption, which are systematically underestimated by the classical slab method, as it neglects fishtail-induced spreading [13]. To overcome this limitation, an analytical formulation that explicitly accounts for lateral spread is proposed in the present work.

**Classical Slab Approach Not Considering Fishtail Defect.**

Fig. 3 represents the cross-sectional view of the rolling gap (Fig. 3a) and the generated driving roll normal pressure (Fig. 3b). The ring enters with a width $w_{in}$ [mm], corresponding to a contact angle $\alpha_{in}$ [rad], and exits from it with a reduced width $w_{out}$ [mm]. As demonstrated in [13], at the angular position $\alpha_n$ [rad], defined as the neutral angle, the normal pressure is maximum, and the driving roll and the ring surface have the same tangential velocity. From $\alpha_{in}$ to $\alpha_n$ – entering area – a friction action $\tau^+(\alpha)$ forcing the ring toward the roll gap, and increasing the required torque is generated. The friction action $\tau^-(\alpha)$ from $\alpha_n$ to exit – exiting area – is instead opposed to the material flow, reducing the total amount of required torque.

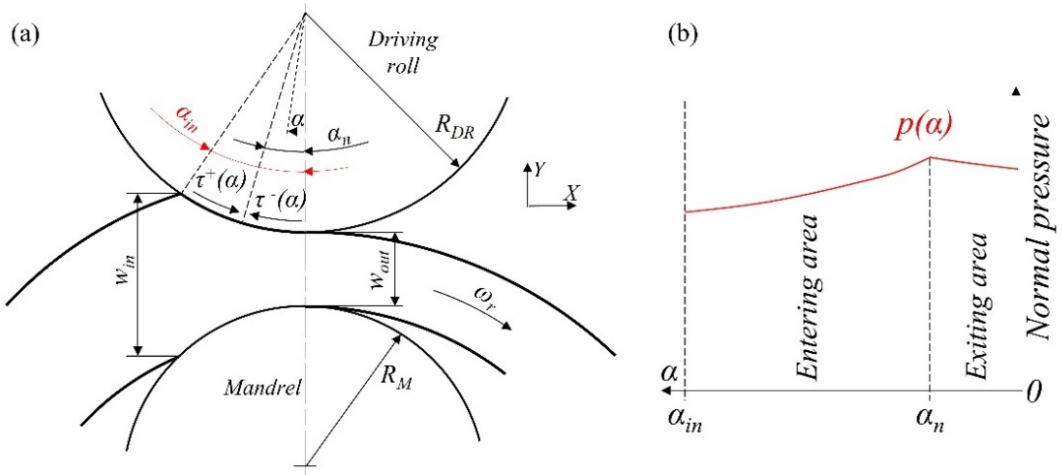


**Fig. 3.** Roll gap cross-section.

The application of slab method allows to determine $\alpha_n$ with Eq. 1 [13]:

$$\alpha_n = \frac{1}{2}\sqrt{\frac{w_{out}}{R_{DR}}} \cdot \tan\left[\tan^{-1}\left(\sqrt{\frac{R_{DR}}{w_{out}}} \cdot \alpha_{in}\right) - \frac{1}{2}\sqrt{\frac{w_{out}}{R_{DR}}} \cdot \frac{\ln\left(\frac{w_{in}}{w_{out}}\right)}{\mu}\right] \quad (1)$$

where $R_{DR}$ [mm] is the driving roll radius, $\mu$ is the friction coefficient at the ring-driving roll interface, and $\alpha_{in}$ is calculated with Eq. 2 [13].

$$\alpha_{in} = \cos^{-1}\left(1 - \frac{w_{in} - w_{out}}{2 \cdot R_{DR}}\right) \quad (2)$$

Considering then the mean normal pressure in the roll gap $\bar{p}$ [MPa] (Eq. 3), instantaneous driving roll torque $T$ [Nm] and total energy $E$ [J] are assessed by Eq. 4 and Eq. 5 respectively, where $h$ is the instantaneous ring height, $\sigma_{eq}$ is the material equivalent stress [MPa], and $t_{RR}$ is the process time [s] (Eq. 6).

$$\bar{p} \cong \frac{\sqrt{2}}{3}\sigma_{eq} \quad (3)$$

$$T = \mu \cdot \bar{p} \cdot h \cdot R_{DR}^2 \cdot \alpha_{in} \cdot \left(1 - \frac{2 \cdot \alpha_n}{\alpha_{in}}\right) \quad (4)$$

$$E = \int_0^t T \cdot \omega_{DR} \cdot dt \quad (5)$$

$$t_{RR} = \frac{w_i - w_f}{f} \quad (6)$$

**Modified Slab Approach Considering Fishtail Defect.**

When the fishtail effect develops, the ring cross-section no longer remains uniform along its height. Instead, the central width $w$ increases progressively toward the axial ends, reaching a maximum value $w^*$ at the interface with the axial rolls (Fig. 2). After half a revolution, this deformed cross-section enters the mandrel–driving roll gap, where it produces a non-uniform contact angle along the ring height. The largest contact angle, denoted as $\alpha_{in}^*$, occurs at the upper and lower edges of the ring at the onset of contact (section A-A in Fig. 4), where the local ring width equals $w_{in}^*$, corresponding to the $w^*$ measured half a rotation earlier. As the material advances toward the exit of the roll gap (section B-B in Fig. 4), both the ring width and the associated contact angle gradually decrease. When the roll gap width matches the central ring width $w_{in}$ – equal to the $w$ value measured half a revolution before – the entire lateral surface of the ring comes into contact with the driving roll. This condition corresponds to the minimum contact angle $\alpha_{in}$ (section C-C of Fig. 4).

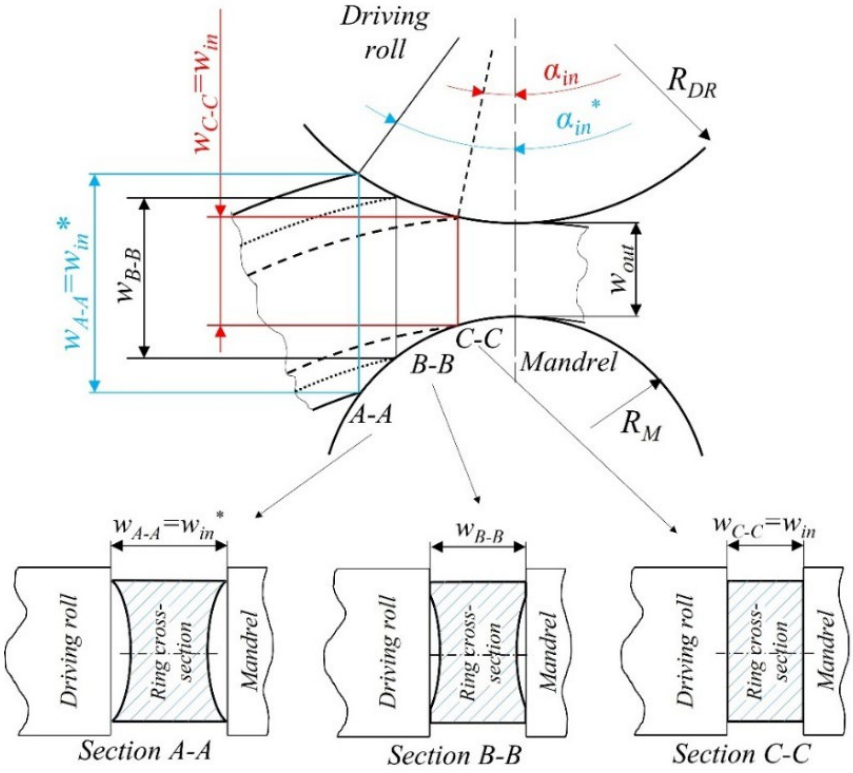


**Fig. 4.** Variability of contact angle along ring height due to the fishtail effect.

The value of $\alpha_{in}^*$ is calculated by substituting $w_{in}$ with $w_{in}^*$ in Eq. 2. The complex shape of the cross-section makes it difficult to evaluate the contact length along ring height. To overcome this limitation, a mean value of $\alpha_{in}^*$ and $\alpha_{in}$, defined as $\overline{\alpha_{in}}$, between, is employed as contact angle. Substituting it in Eq. 1, it is then possible to evaluate the mean values of the neutral angle $\overline{\alpha_n}$. Defining then $t_{hr}$ [s] as the time required for threading half revolution of the ring, the estimation of torque $T^*$ and energy $E^*$, considering the fishtail effect, can be finally carried out by Eq. 7 and Eq. 8, respectively.

$$T^* = \begin{cases} \mu \cdot \bar{p} \cdot h \cdot R_{DR}^2 \cdot \alpha_{in} \cdot \left(1 - \frac{2 \cdot \alpha_n}{\alpha_{in}}\right) & \text{for } t < t_{hr} \\ \mu \cdot \bar{p} \cdot h \cdot R_{DR}^2 \cdot \overline{\alpha_{in}} \cdot \left(1 - \frac{2 \cdot \overline{\alpha_n}}{\overline{\alpha_{in}}}\right) & \text{for } t \geq t_{hr} \end{cases} \tag{7}$$

$$E = \int_0^t T^* \cdot \omega_{DR} \cdot dt = \int_0^{t_{hr}} \mu \cdot \bar{p} \cdot h \cdot R_{DR}^2 \cdot \alpha_{in} \cdot \left(1 - \frac{2 \cdot \alpha_n}{\alpha_{in}}\right) \cdot \omega_{DR} \cdot dt + \int_{t_{hr}}^t \mu \cdot \bar{p} \cdot h \cdot R_{DR}^2 \cdot \overline{\alpha_{in}} \cdot \left(1 - \frac{2 \cdot \overline{\alpha_n}}{\overline{\alpha_{in}}}\right) \cdot \omega_{DR} \cdot dt \tag{8}$$

## Material and Methods

To validate the proposed model, its results were compared with the ones obtained from a RR FEM simulations campaign previously verified by the authors [11]. The FEM campaign was performed by means of Deform 3D software (SFTC, Ohio, US) and concerned the ring rolling process of an industrial bearing component made of AISI 1045 carbon steel. The driving roll had a radius $R_{DR}$ of 350 mm, the mandrel radius $R_M$ was 55 mm, and the conical axial rolls were 400 mm height with a taper angle of 15.7 °. Table 1 reports initial and final dimensions of the ring.

**Table 1.** Main dimensions of the ring.

| Geometric parameter | Initial dimensions | Target/final dimensions |
|---|---|---|
| External diameter | $D_i$ = 258 [mm] | $D_f$ = 387.39 [mm] |
| Internal diameter | $d_i$ = 120 [mm] | $d_f$ = 279.79 [mm] |
| Width | $w_i$ = 69 [mm] | $w_f$ = 53.8 [mm] |
| Height | $h_i$ = 75 [mm] | $h_f$ = 54.5 [mm] |

A total number of 15 simulations were performed by combining three levels of $f$ (1.00; 1.25; 1.50 [mm/s]) and five levels of $\omega_r$ (5; 10; 15; 20; 25 [rad/s]), maintained constant during each test. The axial roll motion law $f_{AR}$ was defined by Eq. 9, allowing the determination of instantaneous width $w$ and height $h$ of the ring with Eq. 10 and Eq. 11, respectively:

$$f_{AR} = \frac{f}{2} \cdot \frac{h_i - h_f}{w_i - w_f} + f^2 \cdot \frac{h_i - h_f}{(w_i - w_f)^2} \cdot t \tag{9}$$

$$w = w_i - \int_0^t f dt = w_i - f \cdot t \tag{10}$$

$$h = h_i - \int_0^t f_{AR} dt = h_i - f \cdot \frac{h_i - h_f}{w_i - w_f} \cdot t \cdot \left(1 + \frac{f}{w_i - w_f} \cdot t\right) \tag{11}$$

The value of $\omega_{DR}$ required for maintaining the ring at a constant speed $\omega_r$, was then calculated by considering ring volume constancy (Eq. 12).

$$\omega_{DR} = \frac{\omega_r}{R_{DR}} \cdot \frac{D}{2} = \frac{\omega_r}{2 \cdot R_{DR}} \left[w + \frac{h_i \cdot w_i \cdot (D_i - w_i)}{h \cdot w}\right] \tag{12}$$

A zero-resistance torque condition was imposed on both the mandrel and the axial rolls. All machine components were modeled as perfectly rigid, whereas the ring was assigned the viscous–plastic material model for AISI 1045 steel available in the software database. Interactions between the ring and the forming tools were defined using a limiting shear stress friction model. The simulations were conducted under isothermal conditions, with the ring temperature set to 1150 °C. Further details regarding the FEM configuration are reported in [11].

Torque peaks and energy associated with the driving roll were extracted from the simulations and compared with the predictions of both the classical and the modified analytical models. In addition, the final spread difference $\Delta w_f^*$ obtained at the end of each simulation was measured and subsequently used to estimate the evolution of $\Delta w^*$ throughout the RR process, as further described.

## Implementation of the Proposed Methodology

The mechanistic model accounting for the fishtail effect emphasizes the need to determine the instantaneous spread difference $\Delta w^*$. Considering that $\Delta w^*$ increases during the RR process [12], as a first approximation, this work hypothesizes a linear growth of $\Delta w^*$ during time. Therefore, once the spread difference at the end of process $\Delta w_f^*$ is known, its evolution can be assessed with Eq. 13:

$$\Delta w^* = w + \Delta w_f^* \cdot \frac{t}{t_{RR}} \tag{13}$$

Considering the significance of the kinematic ratio $k_r$, – the ratio between $f$ and $\omega_r$ – on the lateral spread [10], the behavior of $\Delta w_f^*$ from FEM simulations was plotted as a function of $k_r$ (Fig. 5). The strong influence of $k_r$ on the fishtail effect is observable. As $k_r$ increases, the lateral spread also increases, exhibiting a parabolic trend. Consequently, a quadratic regression was employed to determine $\Delta w_f^*$, resulting in Eq. 14 with a $R^2$ equal to 0.9911, confirming the model's good fitting capability.

$$\Delta w^* = 132.29 \cdot k_r^2 + 9.2815 \cdot k_r \tag{14}$$

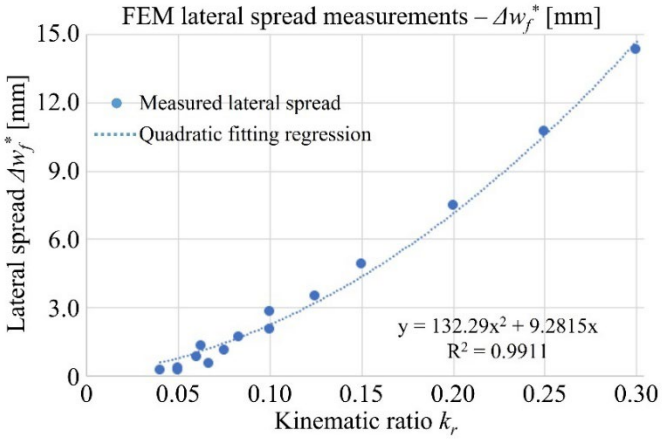


**Fig. 5.** Final lateral spread difference $\Delta w_f^*$ vs. $k_r$ and quadratic fitting regression curve.

The governing equations of the previously introduced models were implemented in a custom Matlab®-based software to compute the evolution of torque and energy. The overall computational workflow, illustrated in Fig. 6, includes calculations performed both with and without accounting for the fishtail effect. In accordance with [14] for hot rolling conditions, the friction coefficient μ was set to 0.6. All time-dependent variables were evaluated at each time increment $\Delta t$. To ensure an adequate temporal discretization of the process, $\Delta t$ was selected as the time required for the ring to complete one fifteenth of a full revolution. During the initial computation stage, the variables $w$, $h$, $f_{AR}$, $\omega_{DR}$, and the number of ring revolutions $N_{rev}$ [rev] (Eq. 15) were updated iteratively until the total rolling time $t_{RR}$ was reached. Simultaneously, the radial $\varepsilon_y$, axial $\varepsilon_z$, and circumferential $\varepsilon_x$ strain components were calculated assuming perfectly plastic and incompressible material behavior (Eq. 16). These strain components were then used to determine the equivalent strain $\varepsilon_{eq}$ (Eq. 17) and the corresponding equivalent strain rate $\dot{\varepsilon}_{eq}$ (Eq. 18).

$$N_{rev} = \frac{\omega_r}{2\pi} \cdot t \tag{15}$$

$$\begin{cases} \varepsilon_x = -(\varepsilon_y + \varepsilon_z) \\ \varepsilon_y = \ln \frac{w_i}{w} \\ \varepsilon_z = \ln \frac{h_i}{h} \end{cases} \tag{16}$$

$$\varepsilon_{eq} = \sqrt{\frac{2}{3}\left(\varepsilon_x^2 + \varepsilon_y^2 + \varepsilon_z^2\right)} \tag{17}$$

$$\dot{\varepsilon_{eq}} = \sqrt{\frac{2}{3}\left(\dot{\varepsilon_x^2} + \dot{\varepsilon_y^2} + \dot{\varepsilon_z^2}\right)} \frac{\omega_r}{2\pi} \cdot t \tag{18}$$

This permits to determine $\sigma_{eq}$ and $\bar{p}$, employing the material flow stress of Eq. 19 [15] with a temperature $\theta$ equal to 1150 [°C].

$$\sigma_{eq} = \left(64.36 + 499.9\varepsilon_{eq} - 940.3\varepsilon_{eq}^2\right)\left(1 + 0.1061 \ln \dot{\varepsilon_{eq}}\right) e^{\left[\left(-0.00359 + 8.73 \times 10^{-5} \ln \dot{\varepsilon_{eq}}\right) \cdot (\theta - 1223)\right]} \tag{19}$$

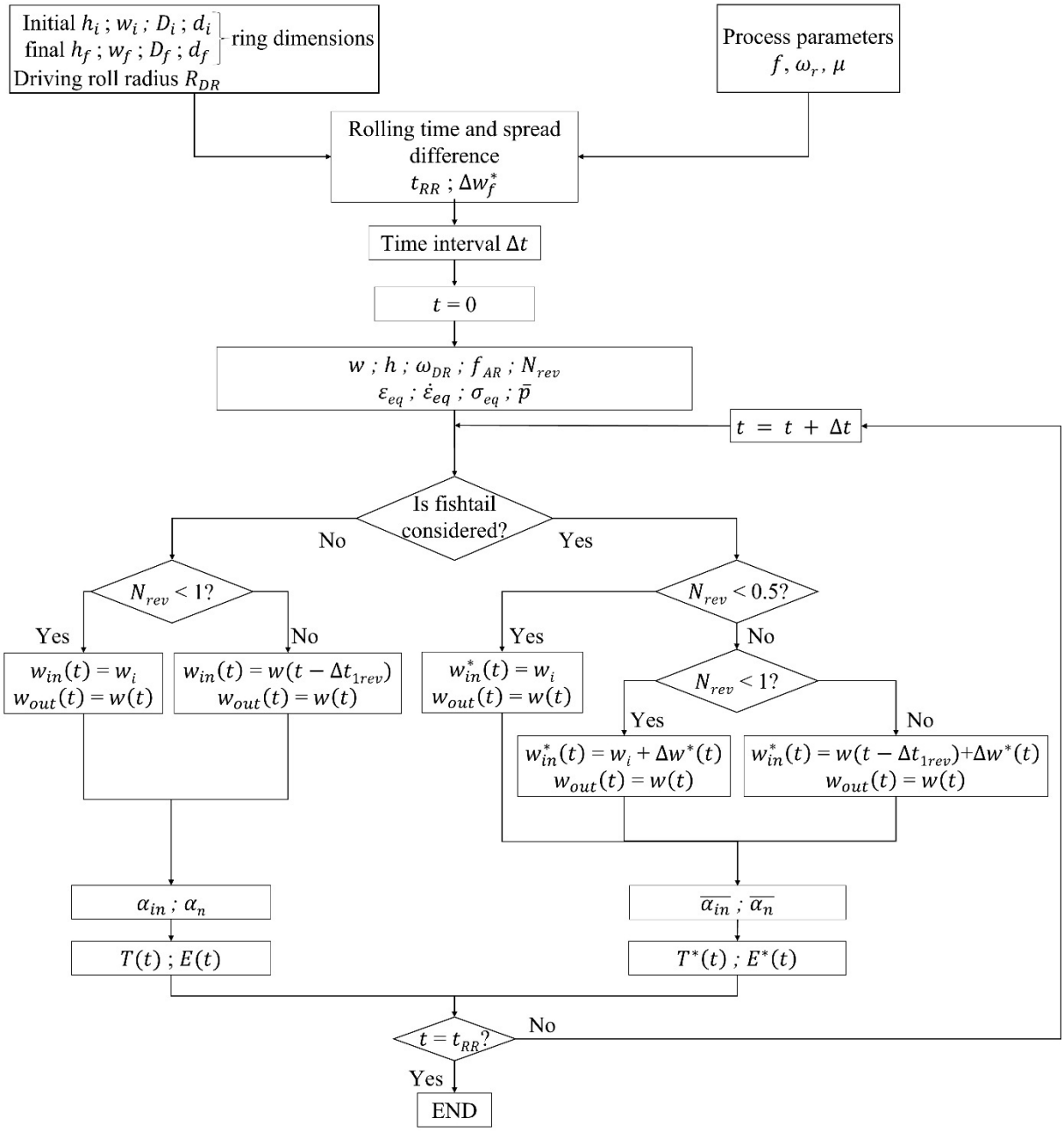


**Fig. 6.** Adopted workflow for ring rolling torques and energies calculation.

Subsequently, the algorithm computes torque and energy using either the classical or the modified slab formulation. When the classical slab method is adopted, the instantaneous ring width at the entry of the mandrel–driving roll gap, $w_{in}(t)$, remains equal to the initial width $w_i$ until the ring completes one full revolution ($N_{rev} = 1$). After this point, the entry width $w_{in}(t)$ is updated as the exit width from the preceding revolution $w_{in}(t - \Delta t_{1rev})$, where $\Delta t_{1rev}$ denotes the time required for a single ring revolution. In all cases, the instantaneous exit width is equal to the current ring width $w(t)$. When the modified slab method is employed, the instantaneous entry width $w_{in}^*(t)$ remains equal to $w_i$ until half a ring revolution is completed, corresponding to the moment when the deformed cross-section first reaches the roll gap. From that instant onward, $w_{in}^*(t)$ is defined as the sum of the initial width $w_i$ and the instantaneous spread difference $\Delta w^*(t)$, since $N_{rev}(t) = 1$. After one full revolution, the entry width is updated as the sum of the instantaneous spread difference $\Delta w^*(t)$ and the exit width from the previous revolution $w_{in}(t - \Delta t_{1rev})$. As in the classical formulation, the exit width in the modified approach remains equal to $w(t)$. Once the temporal evolutions of the entry and exit ring widths have been determined for both formulations, the instantaneous contact angle, neutral angle, and contact length are evaluated, allowing the corresponding torque to be calculated. Owing to the

discrete implementation of the model, the evolution of energy, $E(t)$ or $E^*(t)$, is obtained by a Riemann summation of the product of torque, $T(t)$ or $T^*(t)$, and the driving roll angular velocity over time, as expressed in Eq. (20).

$$E(t) = \sum_{\Delta t=0}^{t} \frac{[T(t)+T(t-\Delta t)]\cdot[\omega_{DR}(t)+\omega_{DR}(t-\Delta t)]}{2} \cdot \Delta t \tag{20}$$

## Results and Discussion

Fig. 7a shows the maximum values of torques $T_{MAX}$ resulting from simulations (Δ), slab approach (X), and the proposed modified slab method (O). Accordingly, Fig. 7b plots the values $E$. The good superposition of torques and energies when the proposed methodology is applied is observable.

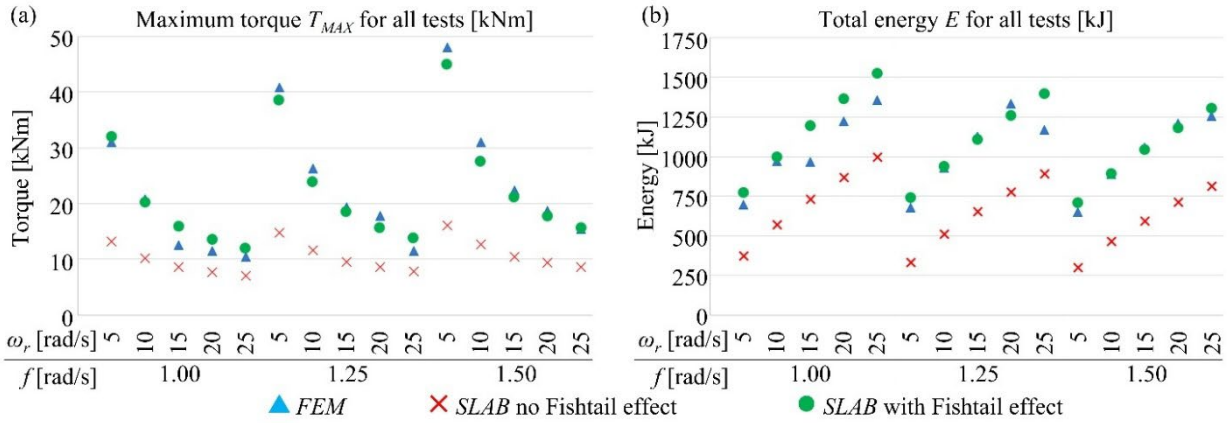


**Fig. 7.** Summary of (a) torque maximum values and (b) energy.

The percentage errors $e_{\%}$, correlated to the two analytical models respect to the FEM results, in the calculation of torque and energy peaks, are reported in figure 8a and figure 8b respectively.

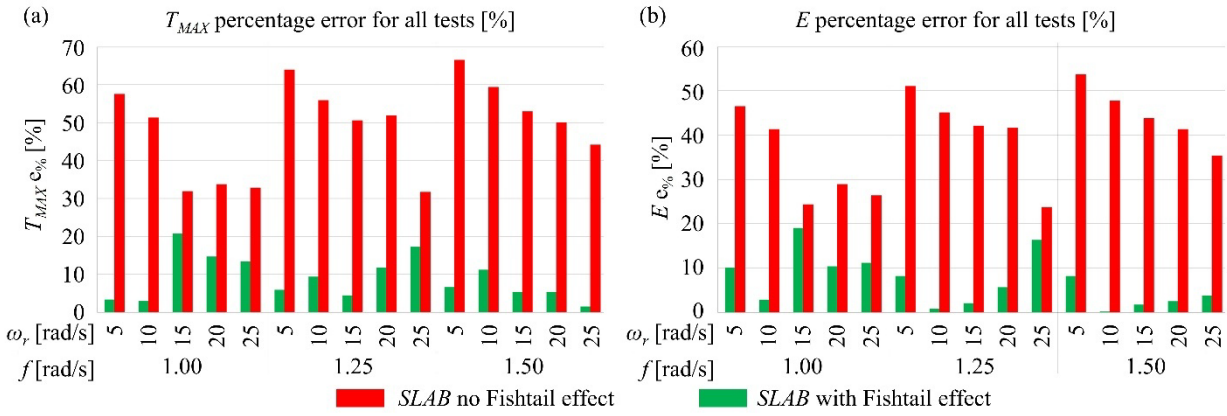


**Fig. 8.** Percentage errors in torque and energy analytical calculations for all the tests.

The errors of the analytical model not considering the fishtail effect underline its inadequacy, showing unacceptable errors reaching values greater than the 60 % and the 50 % for torque peaks and energy respectively. On the contrary, when the model concerning the fishtail effect is applied, the errors are lower than 15 %, with only some exceptions. These are mainly related to tests characterized by low values of $k_r$ – $f$ = 1.25 mm/s and $\omega_r$ = 25 rad/s with $k_r$ = 0.050; $f$ = 1.00 mm/s and $\omega_r$ = 15 rad/s with $k_r$ = 0.067 – where a high dispersion of the values around the curve of Fig. 5 is observable. This causes a bad approximation of $\Delta w_f^*$, resulting in a wrong calculation of the mean contact angle that, in turn, reduces the accuracy of torque and energy assessment. To overcome the limitations related to the employment of Eq. 14 for estimating $\Delta w_f^*$, further studies on lateral spread behavior will be performed.

Fig. 9 shows torque and energy evolutions for the tests giving the lowest percentage errors – namely $f$ = 1.50 mm/s, $\omega_r$ = 25 rad/s for torque (Fig. 9a) and $f$ = 1.50 mm/s, $\omega_r$ = 10 rad/s for energy (Fig. 9b). The good match along the process time is detectable, underlining the capability of the proposed modified slab approach in forecasting torque and energy behavior.

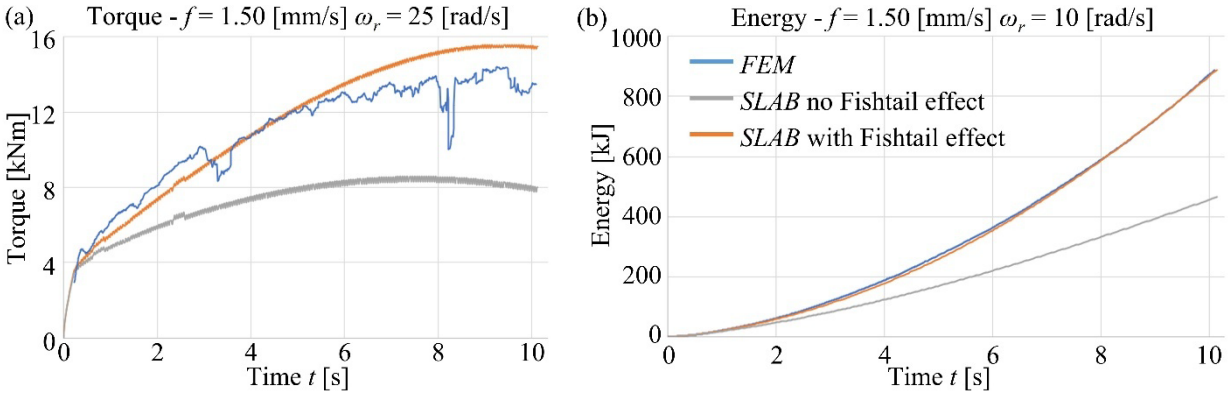


**Fig. 9.** Torque (a) and energy (b) evolution for the lowest percentage error tests.

## Conclusion

This study proposed and validated a new analytical methodology for torque and energy estimation in ring rolling processes, considering the fishtail effect. The model combines the classical slab approach with a regression-based evaluation of lateral spread as a function of the kinematic ratio, thereby extending the predictive capability of analytical formulations.

The methodology was benchmarked against an industrial FEM simulation campaign, showing that neglecting the fishtail effect leads to severe inaccuracies, with torque and energy prediction errors exceeding 60% and 50%, respectively. In contrast, the proposed model drastically reduced such deviations, achieving errors below 15% in the majority of tests. Cases with higher discrepancies were associated with limitations in the regression approximation or FEM fluctuations rather than intrinsic weaknesses of the model.

Overall, the proposed framework enables accurate, efficient, and robust prediction of ring rolling mechanics without the need for computationally intensive FEM analyses. Its integration into process design tools can support industrial applications by providing quick and reliable estimations of torque and energy.

## References

[1] H. He, Y. Yi, S. Huang, Y. Zhang, An improved process for grain refinement of large 2219 Al alloy rings and its influence on mechanical properties, J. Mater. Sci. Technol. 35 (2019) 55–63.

[2] J.T. Yeom, J.H. Kim, N.K. Park, S.S. Choi, C.S. Lee, Ring-rolling design for a large-scale ring product of Ti–6Al–4V alloy, J. Mater. Process. Technol. 187–188 (2007) 747–751.

[3] J.B. Hawkyard, W. Johnson, J. Kirkland, E. Appleton, Analyses for roll force and torque in ring rolling, with some supporting experiments, Int. J. Mech. Sci. 15 (1973) 873–893.

[4] G. Allegri, L. Giorleo, E. Ceretti, C. Giardini, Driver roll speed influence in Ring Rolling process, Procedia Eng. 207 (2017) 1230–1235.

[5] C. Cappellini, C. Giardini, S. Bocchi, A multi-objective optimization workflow of ring-rolling process parameters based on production energy and time, Procedia CIRP 122 (2024) 683–688.

[6] N. Kim, S. Machida, S. Kobayashi, Ring rolling process simulation by the three dimensional finite element method, Int. J. Mach. Tools Manuf. 30 (1990) 569–577.

[7] L. Quagliato, G.A. Berti, D. Kim, N. Kim, Slip line model for forces estimation in the radial-axial ring rolling process, Int. J. Mech. Sci. 138–139 (2018) 17–33.

[8] D. Xie, Y. Wang, Q. Ouyang, L. He, W. Xu, Analytical calculation model for radial-axial coordinated feed strategy in large-scale flat ring rolling based on ultimate bending moment, J. Mater. Process. Technol. 319 (2023) 118072.

[9] W. Johnson, G. Needham, Experiments on ring rolling, Int. J. Mech. Sci. 10 (1968) 95–113.

[10] H. Zayadi, A. Parvizi, H.R. Farahmand, D. Rahmatabadi, Investigation of Ring Rolling Key Parameters for Decreasing Geometrical Ring Defects by 3D Finite Element and Experiments, Arab. J. Sci. Eng. 46 (2021) 12105–12115.

[11] C. Cappellini, L. Giorleo, Ring rolling with flat dies: An analytical method to optimize geometry, time or energy, J. Mech. Sci. Technol. 38 (2024) 5543–5558.

[12] C.F. Lugora, A.N. Bramley, Analysis of spread in ring rolling, Int. J. Mech. Sci. 29 (1987) 149–157.

[13] W. Johnson, P.B. Mellor, Engineering plasticity, E. Horwood; New York: Halsted Press, Chichester, West Sussex, England, 1983.

[14] S. Kobayashi, Metal Forming and the Finite-Element Method, Oxford University Press, Incorporated, New York, 1989.

[15] M. Murugesan, D. Jung, Johnson Cook Material and Failure Model Parameters Estimation of AISI-1045 Medium Carbon Steel for Metal Forming Applications, Materials 12 (2019) 609.